The DOI for this manuscript is doi: 10.1175/JCLI-D-17-0136.1

The final published version of this manuscript will replace the preliminary version at the above DOI once it is available.

If you would like to cite this EOR in a separate work, please use the following full citation:

Cesana, G., D. Waliser, D. Henderson, T. L'Ecuyer, X. Jiang, and J. Li, 2018: The Vertical Structure Of Radiative Heating Rates: A Multimodel Evaluation Using A-Train Satellite Observations. J. Climate. doi:10.1175/JCLI-D-17-0136.1, in press.

The Vertical Structure Of Radiative Heating Rates: A Multimodel Evaluation Using A-Train Satellite Observations

G. Cesana[1,2,3,4 a)], D. E. Waliser[1], D. Henderson[5], T. S. L'Ecuyer[5], X. Jiang[6], J-L. F. Li[1]

[1] *Jet Propulsion Laboratory, California Institute of Technology, Pasadena, CA, USA*

[2] *Columbia University, Department of Applied Physics and Applied Mathematics, New York, NY*

[3] *NASA Goddard Institute for Space Studies, New York, NY.*

[4] *Columbia University, Center for Climate Systems Research, Earth Institute, New York, NY*

[5] *University of Wisconsin—Madison, Madison, WI, USA*

[6] *Joint Institute for Regional Earth System Science & Engineering, University of California, Los Angeles, CA, USA*

[a)] Corresponding author: Gregory.cesana@columbia.edu

ABSTRACT.

We assess the vertical distribution of radiative heating rates (RHR) in climate models using a model experiment and A-train satellite observations, for the first time. As RHR relies on the representation of cloud amount and properties, we first compare the modeled vertical distribution of clouds directly against lidar-radar combined cloud observations (i.e., without simulator). On a near-global scale (50°S/N), two systematic differences arise: an excess of high-level clouds around 200hPa in the tropics, and a general lack of middle- and low-level clouds compared to the observations. Then, using RHR profiles calculated with constraints from A-train and reanalysis data, along with their associated maximum uncertainty estimates, we show that the excess clouds and ice water content in the upper troposphere results in excess infrared heating in the vicinity and below the clouds as well as a lack of solar heating below the clouds. In the lower troposphere, the smaller cloud amount and the underestimation of cloud-top height is coincident with a shift of the infrared cooling to lower levels, substantially reducing the greenhouse effect, that is slightly compensated for by an erroneous excess absorption of solar radiation. Clear sky RHR differences between the observations and the models mitigate cloudy RHR biases in the low levels while they enhance them in the high levels. Finally, our results indicate that a better agreement between observed and modeled cloud profiles could substantially improve the RHR profiles. However, more work is needed to precisely quantify modeled cloud errors and their subsequent effect on RHR.

1. INTRODUCTION

Clouds strongly interact with radiation and modulate the amount of energy reflected, emitted and absorbed by the Earth system. This redistribution of energy within the troposphere has implications for climate prediction, as it impacts the large-scale circulation, vertical motions and atmospheric water cycle (e.g. Stephens et al., 2012). As the earth warms, the spatial distribution of clouds changes, leading to a modification of the energy balance. Based on sensitivities to cloud height, the temperature and microphysical properties of a cloud may change drastically. In turn, its radiative effects may therefore be considerably different and result in either a warming or a cooling of the atmospheric layer (e.g. Ackerman et al., 1988). For example, the warming generated by a cirrus cloud in the layers underneath can be large enough to cancel out the ascent of air motion generated by the Hadley circulation (e.g. Mather et al., 2007). In addition, in climate modeling and projection, cloud-radiation interactions are particularly important as they drive the cloud-climate feedbacks that strongly influence a range of climate system behaviors (e.g. Brient and Bony, 2012).

While passive sensor satellites have been monitoring the outgoing and incoming radiative fluxes at the top of the atmosphere for years (e.g. Wielicki et al., 1996), observations of the vertical profile of radiative heating is still largely unconstrained, which affects our ability to better understand and model the present and future climate (e.g. Stephens et al., 2012). For example, Mace and Wrenn (2013) showed that for a similar top-of-atmosphere (TOA) radiative signature, clouds can have very different vertical profiles and therefore heating rate profiles, leading to diverse surface radiative forcings. Since 2006, measurements of the global cloud frequency (CF) and radiative fluxes at relatively high resolution have been made possible by active sensors onboard the Cloud-Aerosols Lidar and Infrared Pathfinder Satellite Observations (CALIPSO; Winker et al., 2010) and the CloudSat satellite (Stephens et al., 2002) flying in the A-Train constellation. For example, using CALIPSO measurements, Chepfer et al. (2010) developed a General Circulation Model (GCM) -oriented cloud product to evaluate climate models (e.g., Cesana and Waliser, 2016). Based on CloudSat measurements and a radiative transfer model, L'Ecuyer et al. (2008) developed a radiative flux retrieval so-called 2B-FLXHR product. This product was later improved by integrating other A-Train satellite measurements (Henderson et al., 2013, hereafter H13) from CALIPSO and Moderate Resolution Imaging Spectroradiometer (MODIS) (King et al., 2003) to take into account the contribution of thin cirrus and near surface shallow/strato- cumulus clouds and aerosols, referred to as the 2B-FLXHR-LIDAR product. These observationally-constrained radiative flux retrievals give us the opportunity to characterize radiative heating features at a vertical resolution much higher than that of passive sensors (Haynes et al., 2013), although their horizontal coverage is sparser. As a consequence, this very unique dataset offers a new resource for climate model evaluation, independent from the traditional observations used to tune models' fluxes at the top of the atmosphere (e.g., Hourdin et al., 2016).

Some "observation-based" studies have shown the usefulness of these datasets to investigate the impact of cloud occurrences in vertical profiles of heating rates (e.g., Thorsen et al., 2013) as well as microphysical properties of clouds (e.g., Waliser et al., 2011), or to determine which layer of the atmosphere was contributing the most to the cooling/warming of the column (e.g., Oreopoulos et al., 2016) or even to validate ground-based measurements (e.g., Protat et al., 2014). However, because the Cloud Model Intercomparison Project phase 5 (CMIP5, Taylor et al., 2012) did not require participating modeling groups to output radiative heating rates (RHR), very few studies have yet to take advantage of the 2B-FLXHR-LIDAR product to assess the representation of vertical structure of RHR in climate models. Fortunately, a recent multimodel climate experiment co-sponsored by the Global Energy and Water Cycle Exchange (GEWEX) Project's

Atmosphere System Study (GASS) Program and the Madden Julian Oscillation Task Force under the Year of Tropical Convection (YoTC) project (hereafter GASS-YoTC), provides vertically-resolved RHR outputs from a large number of GCMs (Jiang et al., 2015). This makes it possible to assess climate models on a global perspective when compared to A-Train-based RHR product. For example, Li et al. (2016) used the aforementioned models and observations to examine the relation between the models' biases in RHR and biases in winds, water vapor and cloud mass over the tropical Pacific Ocean sector, with a special emphasis on the radiative effect of precipitating hydrometeors. However, to date, no study has documented the effect of models' cloud biases on RHR vertical profiles, particularly from a (near) global perspective.

In this study, we characterize systematic differences in the vertical structure of clouds simulated by GASS-YoTC GCMs (used to derive the modeled RHR profiles), in a direct comparison (i.e., no simulators) against the CloudSat-CALIPSO combined cloud fraction (used to derive the A-train RHR profiles). We then evaluate modeled profiles of RHR against A-Train-based datasets on a global scale, for the very first time, and analyze how the differences in cloud profiles may affect the modeled RHR profiles. We describe the different model experiments and observational datasets in Section 2, the results in Section 3 and 4. Finally, we present our conclusions in Section 5.

2. DATASETS AND MODEL EXPERIMENTS

2.1 The 2B-FLXHR-LIDAR radiative heating rates

Description of the product

The 2B-FLXHR-LIDAR product, referred to as 2BFL in the rest of the manuscript, combines CloudSat, CALIPSO, and MODIS observations to generate profiles of RHR at 240 m vertical oversampled and 1.5 km horizontal resolutions. These are computed based on a forward radiative transfer model (see the 2BFL Process Description and Interface Control Document on CloudSat website: http://www.cloudsat.cira.colostate.edu/data-products/level-2b/2b-flxhr-lidar) that is supplied with the CloudSat/CALIPSO combined cloud mask (so-called radar-lidar geometrical profile [RL-GeoProf], Mace and Zhang., 2014), CloudSat microphysical retrievals (Radar Only, 2B-CWC-RO, Austin et al., 2009) and collocated MODIS (2B-TAU) and CALIPSO (Cloud PROfile [CPRO] Level2, version 3, Vaughan et al., 2009) products for clouds and aerosols not detected by the radar. The fluxes are then converted into RHR using the following equation:

$$\frac{dT}{dt} = \frac{g}{C_p}\frac{dF}{dp} \qquad (1)$$

Where T is the temperature (K), t is time (s), g is the acceleration due to gravity (m/s^2), C_p is the specific heat content of air at constant pressure (J/kg.K), F is the radiative flux (W/m^2) and p the pressure (Pa).

In this study, we accumulated nighttime and daytime 2B-FLXHR-LIDAR-R04 granules onto monthly files from 2007 to 2010 over a 2.5°x2.5° horizontal grid and 22 pressure layers from 50hPa to 1000hPa. As the intensity of solar radiation varies with the solar zenith angle, the short wave (SW) RHR is very sensitive to the diurnal cycle (null at night and maximum at noon, solar time). The SW RHR are thus normalized at every level by the matching (in time and space) averaged incoming SW flux at TOA every month, then multiplied by the annual mean climatology of Clouds and the Earth's Radiant Energy System TOA SW flux (2001-2014, version 4.0) to preserve the unit. This takes into account the fact that A-Train measurements are always collected at 13:30 local time. Using this method rather than that of L'Ecuyer et al. (2008) and Ham et al. (2017) does not impact the results significantly (not shown).

Uncertainty analysis

Using CERES fast LW and SW flux dataset (FLASHFlux, Stackhouse et al., 2006) collocated with CloudSat-CALIPSO footprint and sensitivity studies on input parameters of the algorithm, H13 quantified bulk uncertainties in the SW and longwave (LW) 2BFL radiation. Most of the differences are systematic and the largest are found in the downward surface fluxes. At the surface, CERES flux dataset might have larger uncertainties than the 2BFL product on an instantaneous scale for two main reasons. First, it does not benefit from the 3D structure of active sensor, which may add an uncertainty of 12 Wm^{-2} in the global mean surface fluxes (Kato et al., 2012). In particular errors in the cloud base height may generate substantial uncertainties in the surface fluxes (e.g., H13) and better constraining the cloud base height therefore reduces the surface flux uncertainty (e.g., Mulmenstadt et al., 2018). Second, its sensitivity to thin cirrus cloud does not allow to detect clouds with optical thickness smaller than ~0.3 or 0.4 (e.g., Minnis et al., 2008, Ackerman et al., 2008), which occur in up to ~50% of MODIS clear-sky pixels (Sun et al., 2011). For example, classifying cirrus-contaminated pixels as clear sky results in non-negligible biases in the CERES-EBAF SW fluxes (both at the TOA and the surface, e.g., Sun et al., 2011 and H13). In addition, partially-filled clouds due to the larger swath of CERES cloud mask compared to the 2BFL product may generate differences in the cloud fraction of the two datasets (e.g., Zhao and Di Girolamo, 2006, Minnis et al., 2008) and, in turn, affect the retrieved fluxes. This is why differences against CERES estimates at an instantaneous scale cannot be considered as “true” biases although when averaged over large spatial-temporal scales the random errors largely decrease (e.g., H13, L’Ecuyer et al., 2008). However, a constant bias occurs at the surface in the SW clear sky flux against CERES surface dataset, consistent with an independent comparison of clear sky SW RHR between 2BFL and ground-based observations (not shown). It is partly due to errors in surface and land reflectance, as identified by Matus and L’Ecuyer (2017), which decreases the SW absorption. To address this issue, we apply an arbitrary correction of 0.1 K/day to the clear sky SW RHR for every layer, which was chosen to match clear sky CERES surface observations (not shown, see also Fig. 11 in H13) and clear sky RHR profiles from independent ground-based observations (Thorsten et al., 2013; not shown) - because this is a systematic difference it does not change the shape and variability of the 2BFL clear sky SW RHR. They also showed that increasing the carbon dioxide concentrations from 330 ppm to 390 ppm reduces the global outgoing LW radiation by 1.3W/m^2. Finally, using one GCM (IPSL5B), we show in the supporting information (SI) that the spatio-temporal sampling of CloudSat-CALIPSO may generate +/- 0.1 K/day differences in SW and LW vertical RHR (Fig. S1). However, depending on the strength of the GCM’s diurnal cycle, the numbers may slightly fluctuate. These biases are significantly smaller than the model-to-obs differences found in Sec. 4, but may help us explain part of it.

Here we further investigate the maximum uncertainty that could be generated by errors in parameters used as inputs in the 2BFL algorithm to compute the RHR. Following H13 sensitivity experiments, we perturb a set of parameters (Table 1) that have been shown to affect the TOA and surface fluxes the most by H13 and we analyze the effect of these perturbations on the vertical structure of the RHR by taking the square root of the sum of square uncertainties and neglecting covariance between fluxes. Because it is a computationally expensive exercise, we ran the perturbations over a month only, August 2007, as in H13. We first focus on for three cloud regimes (Fig. 1) - later used in Section 4.1 - defined by the value of the large-scale vertical velocity (ω_{500}) and their latitudes: convection (ω_{500} < -10 hPa/day) or subsidence (ω_{500} > 10 hPa/day) in the tropics (between 30˚N/S) and all vertical velocities in the midlatitudes.

In clear sky, the SW RHR error (Fig. 1d-j-p) is driven almost exclusively by errors in the specific humidity regardless of the regime (up to +/- 0.03 K/day). For the LW radiation (Fig. 1c-i-o), both the temperature and the specific humidity produce significant errors. Their magnitude in the middle and high levels is nearly identical and relatively small compared to the lower layers, where the specific humidity dominates the error in the upper part of the boundary layer (up to +0.4 and -0.3 K/day) and the temperature takes over near the surface and to a larger extent (up to +/-0.5 K/day). In cloudy sky, only the specific humidity has a non-negligible impact on the LW and SW RHR (Fig. 1e-k-q and 1f-l-r) while the temperature only impacts the LW radiation. In addition, the two other main contributors to the SW and LW RHR errors are the perturbations of the water contents, which likely affect the cloud's opacity: ice for convective regimes (in the high levels, Fig. 1e-f), liquid for subsidence (in the low levels, Fig. 1k-l) and both at midlatitudes (Fig. 1q-r). However, the impact of changes in the LWC remains small compare to that of IWC because the opacity of liquid clouds is already large. In the all sky (Fig. 1a-b-g-h-m-n), the maximum uncertainty estimates combine all features, which, in some instances, may compensate each other and result in smaller errors. Finally, we study the zonal distribution of the maximum uncertainty estimates, which summarizes the uncertainty analysis (Fig. 2). The largest uncertainties come from either the high levels, driven by IWC perturbations, or the low levels driven by the temperature perturbation near the surface and a combination of the specific humidity and the LWC perturbations in the upper part of the boundary layer.

In conclusion, we remind the reader that these maximum uncertainty estimates are not true uncertainties. For example, the temperature and ERA interim humidity profiles employed in the 2BFL algorithm show a very good agreement with independent observations, even better than other reanalysis datasets (e.g., Kishore et al., 2011, Simmons et al., 2010). Simmons et al. (2010) showed differences in surface temperature smaller than 0.5K over land against in situ observations and smaller than 0.5% for the relative humidity at 2m height. This is far less than the perturbed parameters used to compute maximum errors in the 2BFL sensitivity experiment (+/- 2K and +/- 25%), which are likely larger than the mean error. Therefore, they should not be considered as true uncertainty estimates but rather support our understanding of where the differences against GCMs could come from. Again, we want to emphasize that this maximum combined uncertainty used in the above analysis is probably largely overestimated as it is very unlikely that these sources are all biased (high or low) at the same time. To confirm this, we compared the 2BFL RHR profiles of clear sky conditions with previously published ground-based observations over Darwin (Thorsen et al., 2013). We found negligible differences between our spaceborne observations and the Thorsen et al. (2013) ground-based observations (not shown). In cloudy sky conditions, both the ground-based and spaceborne observations show a very good agreement at levels where the instruments detect similar amount of clouds (i.e., middle and low levels; not shown) and some larger disagreements in high levels, due to differences in cloud fraction and cloud properties.

The RHR products depend on many input parameters, which makes them subject to large uncertainties as demonstrated in this section. However, the uncertainty related to cloud frequency and cloud height is not treated here although it has been shown to produce significant differences among HR datasets (e.g., Ham et al., 2017; Thorsen et al., 2013). To address this and to provide additional insights on the observational uncertainty, we compare the models RHR profiles in section 4.1 with not only the 2BFL observations but also with composite observations resulting from the average of two RHR products (referred to as the merged product): 2BFL and CERES-CALIPSO-CloudSat-MODIS (CCCM, Kato et al., 2010, Ham et al., 2017), which is presented in the section 2.2 hereafter. However, because we do not have maximum uncertainty estimates for the CCCM RHR, we do not use them in the full analysis.

2.2 The CCCM radiative heating rates

In our study, we accumulated nighttime and daytime CCCM granules onto monthly files from 2007 to 2010 over a 2.5°x2.5° horizontal grid and 22 pressure levels from 50hPa to 1000hPa, similar to 2BFL and the GASS-YOTC models. As for 2BFL, the CCCM algorithm also combines information from CloudSat (2B-CLDCLASS, Sassen and Wang, 2008; 2B-CWC-RO), CALIPSO (CALIPSO L2 Vertical Feature Mask [VFM] and CPRO products, Vaughan et al., 2009) and CERES-MODIS (Minnis et al., 2011) observations to derive RHR. However, we may describe it as being independent of the 2BFL product for several reasons. The input parameters used in the CCCM algorithm come from different products than for the 2BFL algorithm, except for CloudSat 2B-CWC-RO and CALIPSO CPRO, which provides ice and liquid water contents and effective radius for radar-only clouds and cloud extinctions for lidar clouds, respectively, in both products.

In addition, they use a different radiative transfer code (Fu and Liou, 1993), a different re-analysis product for the environmental parameters (Rienecker et al., 2011), the CCCM resolution is enhanced to that of CERES and the CCCM profiles are collocated on the CERES footprint (see Ham et al. [2017] for more details).

To summarize, the main differences between the two products lie in the cloud occurrences mostly (along with their height), the water contents and the cloud extinctions to some extent. Although RHR differences in zonally-averaged profiles may be larger than uncertainty estimates found in section 2.1 (Ham et al., 2017, see also see Fig. S2), the main reason is not necessarily due to uncertainties in cloud occurrences and extinctions. In the LW, these large differences (up to 0.9 K/day) result from differences in height of the LW cooling and warming while the patterns and overall values of the two products are fairly similar (within the range of uncertainty found in section 2.1, Fig. S2, and also Fig. 5a-e). A similar statement can be done in the SW, although differences of SW warming at high levels in the tropics are larger than the uncertainty estimates provided in section 2.1 (0.3 K/day vs. 0.1 K/day, Fig. S2), in this particular case likely due to larger cloud extinction in CCCM product (Ham et al., 2017). Therefore, comparing the models with the 2BFL+CCCM merged observations in addition to 2BFL and its uncertainty estimates - as in section 4.1 - provides a kind of observational envelope that takes into account the uncertainty related to cloud properties, cloud occurrences and environmental properties.

2.3 The model experiments

The modeled profiles of RHR for total, clear and cloudy sky come from 5 models that participated in the GASS-YOTC experiment (Jiang et al., 2015; Klingaman et al. 2015). The RHR are outputted 6-hourly and projected onto a 2.5°x2.5° horizontal grid from 50˚S to 50˚N and over

22 standard pressure levels (from 1000hPa to 50hPa). We further averaged into monthly means for an 18-year period. Averaging over a long period of time allows mitigating the impact of clouds and climate pattern oscillations (e.g., El Nino-Southern Oscillation, Madden-Julian Oscillation). However, to provide a sense of the sensitivity of our results to the model record length, we compared the first and last three years of the multimodel simulations against the observations and we found identical biases (not shown). The sea-surface temperature (SST) is prescribed except for one coupled models out of the five GCMs.

Finally, the spatio-temporal uncertainties due to the satellite overpass that is not reproduced in the models are discussed by Cesana and Waliser [2016] in detail in their supplementary information (see also Chepfer et al., 2010). They are negligible compared to the model-to-obs biases (uncertainty<1%).

2.4 The model-to-obs comparison

While the RHR from 2BFL are not direct measurements, they are intended to represent the reality as much as possible. This is why 2BFL uses both lidar and radar cloud information. As a result, it is directly comparable to the models' output of RHR such as one would do for the temperature or flux fields, provided that the uncertainty of the measurements is addressed (as described in the previous Section 2.2).

The cloud information used to produce the observed and modeled RHR are based on the RL-GeoProf dataset (Mace and Zhang, 2014) and the original modeled cloud fraction (i.e., without using any simulator), respectively. Therefore, we compare directly the RL-GeoProf vertical cloud fraction as well as 2BFL liquid and ice water contents with the GASS-YOTC models counterparts to help us interpret the differences between observed and modeled RHR. The RL-GeoProf cloud fraction is computed using 2B-GEOPROF and 2B-GEOPROF-LIDAR products for the same period of time, horizontal and vertical resolution and using the same cloud thresholds as in the 2BFL product. The only way to obtain the 2BFL ice and liquid water contents was to re-run the 2BFL algorithm, which is why we only outputted one year of data (2007) due to limited access to computational resources. Finally, we remind the reader that in such comparison (i.e., no simulator used), limits the evaluation for two main reasons. First, the definition of the cloud among the models and between the models and the observations are different. Second, the limitations of the instruments (e.g., lidar and radar attenuation) are not taken into account in such comparison. As a result, some uncertainties in the cloud comparison remain and prevent us from discussing this in terms of cloud bias. Instead, we point out cloud differences between the 2BFL product and GASS-YOTC models. However, we want to emphasize that both observed and modeled cloud profiles are the ones used to compute their corresponding RHR and thus the differences in the observed and modeled cloudy RHR can be directly linked to cloud differences whether or not these are cloud biases.

3. CLOUD DISTRIBUTION

Contemporary GCMs still struggle to correctly reproduce the climatology of cloud distributions. Using the most recent version of the GCM-Oriented CALIPSO Cloud Product (CALIPSO-GOCCP) and CMIP5/CFMIP2 model's simulations, Cesana and Waliser (2016) showed that two main biases remain in GCMs: too few low clouds (< 3km) and too infrequent high clouds (> 7km) in the column that fill too many upper levels when present (being geometrically too thick). Another common bias is the height of low-level clouds. In the majority of the models, the height of the low-level clouds is typically too low compared to CALIPSO-GOCCP observations, suggesting a boundary layer that is too shallow. Here, we directly compare the RL-GeoProf vertical cloud fraction with the cloud outputs of the file 5 GASS-YOTC models that provides cloudy sky RHR. Such comparison is not free of uncertainties as no simulator is used; however, we remind the reader that the cloud differences found here can be directly linked to cloudy RHR biases.

Figure 3 shows vertical profiles of CF for the RL-GeoProf observations and GASS-YOTC models, which are later used in this study to understand the biases in the modeled cloudy RHR. This comparison is consistent with the main results found in the CMIP5/CFMIP2 model analysis from Cesana and Waliser (2016) – i.e., too many high clouds and too few low clouds - except in two locations. Near the surface around the equator and in the polar regions, the models seem to overestimate the amount of clouds compared to RL-GeoProf observations (Fig. 3d). However, for pressures higher than 900 hPa (i.e., below ~1km), the RL-GeoProf cloud fraction is less accurate due to both radar clutter and to lidar attenuation, therefore any differences at these levels should be treated with caution. In the deep tropics, the models produce slightly less high clouds than RL-GeoProf observations while they simulate more of these when compared with CALIPSO-GOCCP through the lidar simulator (Cesana and Waliser [2016], their Fig. 2). For this type of cloud, the main difference between CALIPSO-GOCCP and RL-GeoProf observations is the detection of the sub-visible cirrus clouds (SVC) with a very small optical thickness (i.e., $\tau<0.03$). The cloud threshold used in CALIPSO-GOCCP and the lidar simulator does not allow to detect SVCs as opposed to the version 3 of the CALIPSO science team product that is used in RL-GeoProf observations. This suggests that the GASS-YoTC models may underestimate the occurrence of thin cirrus clouds in the deep tropics. Another possible explanation is that the five GASS-YOTC models do not suffer from the same bias as the twelve CMIP5/CFMIP2 models.

4. RADIATIVE HEATING RATES

4.1 3D Profiles

Based on the above results, we focus our attention on two specific cloud regimes in this section, defined by the value of the large-scale vertical velocity (ω_{500}) and their latitudes: convection (ω_{500} < -10 hPa/day) or subsidence (ω_{500} > 10 hPa/day) in the tropics (between 30˚N/S). Those are representative of the two main factors driving cloud biases and differences between the observations and the models, which might affect the vertical distribution of the modeled RHR. In addition, we will evaluate the middle latitudes (between 30˚ to 50˚N/S) for all ω_{500}, in which models generally lack of low- and mid-level clouds. Note that for this part of the analysis we excluded the data over land to reduce issues due to vertical interpolation and surface elevation in the models.

4.1.a Convective Regimes

Figure 4-5-6 shows 2BFL (orange lines), merged (purple lines) and multimodel (green lines) mean profiles of RHR over the three aforementioned regimes of interest for cloudy (difference between all and clear sky), all and clear sky conditions (top, middle and bottom rows, respectively). The uncertainty estimates are derived from the same uncertainty estimates as in Fig. 2 but for the specific regimes and regions studied in Fig. 4-5-6. To address the uncertainty due to cloud occurrences, extinctions and height, the merged dataset is used and provide an observational envelope along with the 2BFL product. Note that we specify “2BFL” when we refer to 2BFL observations only. Additionally, the corresponding 2BFL and GASS-YoTC cloud fractions (dark and light black) and ice and liquid water contents (respectively dark and light blue and red) are shown in the top right corner of each figures. Note that similar to the cloud profiles, the observed and modeled ice and liquid water contents are those used to derive the 3D RHR. However, neither a simulator is used in the models, nor uncertainty estimates are provided with the observations, which is why these observed water contents cannot be used to evaluate the models. On the one hand, the Earth atmosphere warms by absorbing SW radiation but not enough to compensate the cooling by LW emission. On the other hand, the clouds slightly modify the picture by enhancing or mitigating the overall cooling.

In regions dominated by convection (Fig. 4), the models simulate slightly more clouds than 2BFL in the high levels, between roughly 200 and 100 hPa (Fig. 4d, grey line, ~5%), and far less below 300 hPa (up to 13%). Coincidently, the models have a larger IWC than 2BFL above 300 hPa, which results in too much LW heating compared to the two observational datasets, consistent with the effect of increasing the IWC in the sensitivity analysis (Fig. 1e, blue and dark blue solid lines). Note that 2BFL IWC is on average 44.3% smaller than 2C-ICE IWC (not shown), which has been shown to be in good agreement with in-situ observations (Deng et al., 2013). This IWC underestimation could affect the 2BFL LW RHR in the high levels. Following our uncertainty analysis, an increasing of the IWC by 70%, larger than the 44.3% difference with 2C-ICE IWC, generates an increase of the LW RHR by up to 0.15 K/day in convective regimes (see Fig. 1a and 1e, solid blue line), which would make it closer to the merged product, but still smaller than the modeled LW RHR. In the low levels, the sensitivity analysis shows that a 50% decrease of the 2BFL LWC (Fig. 1e, red and dark red dashed lines), which roughly corresponds to the modeled LWC below 600 hPa, produces negligible impact on the LW RHR. As a result, one may legitimately think that the substantial lack of LW heating (Fig. 1a, up to 1 K/day) is caused by the lack of clouds in the corresponding low levels.

Contrary to the LW heating, the SW heating falls within the observational envelope (between 2BFL and the merged observations) in the high levels (Fig. 4b). This large SW uncertainty in the observations is related to the cloud ice extinction and optical properties. In CCCM, the extinction coefficients are larger and the ice particle shapes are converted from spherical to non-spherical, which makes them larger and increases their absorption capacity (Ham et al., 2017, their section 5) and may likely generate an overestimation of the SW RHR. Therefore, the real answer likely falls within the two observational estimates of the SW RHR. Below 800 hPa, the cooling is underestimated by the models. Here again, according to the sensitivity analysis, reducing the LWC generate a relatively small decrease of the SW RHR (< 0.01 K/day, Fig. 1b and 1f) in comparison with the larger model bias (0.05 to 0.1 K/day). The scarcity of low-level clouds is therefore likely the main cause of this bias rather than errors in cloud properties such as the LWC.

The modeled net RHR (Fig. 4c) is mainly driven by the LW component and shows the same biases as highlighted above: a significant excess (lack) of warming in the high (low) levels compared to the 2BFL observations and to the merged product in most instances. Finally, in all sky conditions (Fig. 1e), the large lack of LW warming from clouds (~ -1 K/day, Fig. 4a) is partly compensated by a significant lack of LW clear-sky cooling (~ +0.5 K/day, Fig. 4h), in the low-levels. This is likely due to a dry bias in the models, which is consistent with that found by John and Soden (2007), Gonzalez and Jiang (2017) and Wang and Su [2013]. This reduces the water vapor LW cooling, more so in the lowest layers where the water vapor content is the largest. Additionally, larger temperatures near the surface may explain the large decrease of the clear-sky LW cooling in the models, as shown in the sensitivity analysis (Fig. 1c).

4.1.b Subsidence regimes

In subsidence regimes (Fig. 5), a significant amount of clouds are present in the boundary layer with very few overlapping cirrus clouds. This substantial change in the cloud profile tremendously modifies the RHR profiles, particularly in cloudy sky. For this regime, the two observational datasets agree fairly well on the shape of the RHR. The smaller amount of low-level clouds compared to the 2BFL observations (Fig. 5d, grey line, ~ a factor of 2 smaller) likely causes an underestimation of the magnitude of the modeled LW cloud top cooling (Fig. 5a, green line) and reduces the amount of LW radiation emitted to the surface, which therefore weakens the warming underneath the clouds (> 900 hPa). In addition, the low-level cloud-top height is lower in the models than in the 2BFL observations, according to the peak in the cloud fraction. Thus, the cloud top cooling is shifted toward lower levels (compare the green line with the orange and purple lines in Fig. 5a). In the SW (Fig. 5b), the magnitude of the modeled RHR is surprisingly overestimated compared to both observational datasets, despite the simulation of less low-level clouds. As the cloud peak is located further down in the models, it allows more SW radiation to penetrate the lowest layers and increases the SW absorption, despite the smaller amount of cloud and LWC. The combination of these two biases results in an even larger bias in the net RHR (Fig. 5c). Similarly, the LW and SW clear-sky RHR (Fig. 5e-f-g) are too warm in the models and contributes to enhancing the differences with the observations in the all-sky RHR (Fig. 5h-i-j).

4.1.c Midlatitude regimes

In midlatitude regimes (Fig. 6), we find very similar RHR profiles as in the subsidence regimes except in the high-levels wherein the presence of significant amount of clouds generates either a cooling in the LW (Fig. 6a) or a warming in the SW (Fig. 6b). At midlatitudes, high clouds are typically storm-track clouds that are optically thick and extend to the middle levels as opposed to the thinner (both optically and geometrically) cirrus clouds with a higher cloud-top in the deep tropics. Therefore, the storm-track clouds typically cool in the LW, particularly at the cloud top (i.e., between 200 and 400 hPa), and warm in the SW (see Fig. S3). On the one hand, the LW cloud top cooling is slightly underestimated by the models compared to the observations but remains at the edge of the 2BFL maximum uncertainty estimates. This small difference is likely the result of the smaller modeled IWC. On the other hand, the smaller amount of mid-level clouds reduces the SW absorption in the models compared to the observations. In addition, it is interesting to note that in that midlatitudes regime, the low-level cloud amount and height are very similar in both the models and the 2BFL observations (Fig. 6d), which results in lower RHR biases and confirms the importance of getting the correct amount and height of clouds to simulate realistic RHR. Note that the cloud properties contribute less to the bias in the low levels as the liquid clouds are already optically thick. The small differences in the clear-sky RHR profiles (Fig. 6h-i-j) do not impact significantly the all-sky RHR profiles (Fig. 6e-f-g), which mostly fall within the 2BFL uncertainty or the observation envelope.

4.2 Zonal mean analysis

Here we look into the zonal distribution of the RHR from 50˚S to 50˚N to complement the results found in the three specific regimes highlighted above. This model evaluation is performed only against the 2BFL observations, for which we have maximum uncertainty estimates. To highlight significant model error estimates in Fig. 7-8-9, only biases larger than the observed maximum uncertainty estimates are shown (right columns). Finally, to mitigate the biases due to RHR interpolation over land in the models, we apply to all models the surface elevation mask of the ACCESS1.3 model, which is the most conservative. This results in a substantial reduction of the bias over land (not shown).

Figure 7 shows the zonal mean profiles of RHR (LW, SW and net) for the 2BFL observations, the models and their bias in all sky conditions. From both the regime-based and zonal mean analysis, it is quite obvious that the largest biases in the net heating rate are mainly driven by the LW component (bottom row Fig. 7-8-9 and left column in Fig. 4-5-6). Also, the red shading prevails over the blue shading, meaning that the cooling is globally underestimated in climate models. The only significant negative biases are found in the middle levels in areas of deep convection and below 850hPa at all latitudes. The pattern of the biases remains nearly-identical when using 15 models instead of 5 (see Fig. S4) or when compared to the merged product using +/- one standard deviation as an uncertainty estimate (Fig. S5).

The clear sky profiles (Fig. 8) exhibit a large positive bias in the lowest levels, roughly below 800hPa in both the LW and the SW radiation. In the LW, the models' bias is located almost only over ocean and can be attributed mostly to differences in the humidity and temperature profiles, and to a smaller extent, to the lack of carbon dioxide concentration and the satellite sampling differences (Fig. S1) that reduce radiation absorption in the observations particularly in clear sky conditions. Because the amount of water vapor smaller in the lowest layers of the models is underestimated (below 800hPa, Gonzalez and Jiang, 2017, John and Soden, 2007), there is less LW cooling (Fig. 8c). This phenomenon does not affect the SW component as much, which should show slightly less solar absorption (heating, Fig. 8f). The extra-heating around 25˚N in the SW is partly caused by the overestimation of the albedo in the 2BFL observations over desert areas and tropical oceans and differences in aerosol loadings (underestimated by the models) between observations and simulations, which may increase the heating due to water vapor SW absorption (See also Fig. 1d-j-p).

Figure 9 shows zonal profiles of the RHR in cloudy sky conditions, also called cloud radiative effect. In the SW (Fig. 9d-e-f, second row), the observations show a warming in high levels due to SW absorption by high clouds and a cooling in the low levels, generated by a strong reflection of the optically thick low clouds. The pattern is quite well captured by the models: the atmosphere is warmed in the vicinity of the cloud while it is cooled below the cloud base, close to the surface. On the one hand, the cloud differences (e.g. Fig. 3) could cause more SW absorption than in the observations in high levels (Fig. 9f, P ~ 200 hPa in the tropics) – yet within the observations maximum uncertainty - and a significant positive bias close to the surface (P > 800 hPa). On the other hand, they don’t generate as much warming as in the observations in the middle levels and slightly above 400 hPa. When compared to the merged observations, these two main biases – i.e., the lack of warming in the middle levels along with the positive bias below 800 hPa - remain (Fig. S6).

In the LW (Fig. 9, top row), the observed cloud radiative effect in the tropics is less straightforward, which likely results from the averaging of different cloud regimes, in particular the multi-layer clouds, the most frequent in the tropics (e.g., Matus and L'Ecuyer, 2017). However, this specific pattern is consistent with previous studies using both space-borne (Haynes et al., 2013, Oreopoulos et al., 2016, Li et al., 2016) and ground-based observations (Mather et al., 2007, 2009, Protat et al., 2014). The models exhibit significant flaws in the representation of the cloud radiative effect (Fig. 9c). They are not able to simulate the observed cooling around 500 hPa, which is likely generated by a change in microphysical properties of cloud (transition from liquid droplets to ice crystals) at the top of congestus clouds. In addition, they fail to reproduce the warming effect below 500 hPa between 10˚S and 10˚N and between 850 and 950 hPa everywhere. The misrepresentation of the warming effect below 850 hPa outside 10˚S-15˚N is obviously related to the significantly lower occurrence of low-level clouds compared to the observations. However, the lower warming effect toward the base and below the convective clouds (10˚S-15˚N) is less clear. In the observations, this effect likely results from the averaging of different types of cloud, with roughly the same cloud top height but cloud base height ranging from 950hPa to 600hPa. These clouds usually cool the atmosphere at their cloud top and warm toward the base, while having a neutral effect between the base and the top (see Fig. S3). Therefore, this effect is not well represented in the models because they simulate substantially less middle- and low-level clouds in the tropics (Fig. 4d and Fig. 3h-j). In addition, the scarcity of low-level clouds generates cloudier profiles with high-clouds but no underlying low-clouds in the models than in the observations, i.e., low-clouds are less numerous in cloudy profiles. As a result, the warming effect in the low levels is smaller than that observed while the cooling by water vapor is larger. However, the main reason for this bias seems to be the geometric thickness of the clouds. Similar to the SW, we find very similar biases against the merged observations except in the high levels between 10 S/N where the slight excess of warming in the models falls within the observed uncertainty (defined as +/- one standard deviation, Fig. S6).

As in all sky conditions, using the 15 models that provide all sky conditions RHR minus the 5 models that provide clear sky conditions to compute cloudy sky RHR generates very similar biases (see Fig. S7).

5. SUMMARY

In this paper, we use model outputs from the GASS-YOTC project (Jiang et al., 2015) and vertically-resolved measurements of 2BFL CloudSat-CALIPSO-MODIS combined product (H13) to provide for the first time a model evaluation of detailed 3D radiative heating rates (RHR). This was impossible to achieve using traditional TOA and surface flux datasets from passive sensors, which poorly resolve the vertical structure of cloud (e.g., Haynes et al., 2013. Our near-global scale analysis of the all sky RHR as documented by the A-train satellites (along with a radiative transfer model) and as simulated by 5 GASS-YOTC models (Fig. 7) reveals that the LW radiation largely dominates the radiative budget by cooling most of the atmosphere between 50˚S and 50˚N in agreement with what found by Haynes et al. (2013) and Li et al. (2016). Although the SW radiation contributes to a warming of the atmosphere, it is not sufficient to counteract the LW cooling, consistent with previous literature (e.g., Stephens et al., 2012, Trenberth et al., 2009, Wild, 2012).

To perform a fair evaluation of the models, we first address the observational uncertainty by conducting a sensitivity analysis of the 2BFL algorithm to perturbations in input parameters (Fig.

1 and Fig. 2). Because uncertainties related to cloud occurrences are not directly considered in this analysis, we show additional independent RHR observations for comparison in section 4.1 and in the supplementary material for section 4.2 – with slightly different cloud occurrences and extinctions. Based on these results, we further identify biases in the models that are larger than the maximum uncertainty estimates derived from the uncertainty analysis. While the models capture the overall observed features (i.e., LW cooling and SW warming), they suffer from systematic biases and fail to reproduce the detailed vertical structure of the RHR, mostly due to differences in the representation of clouds (Fig. 3, Fig. 4-5-6, top row and Fig. 9). Their ability to reproduce the correct vertical structure of heating rate profiles is indeed tied to their representation of cloud amount and associated properties. The direct comparison of modeled and observed clouds and cloud properties achieved here is not free of uncertainties (e.g., no simulator used), and therefore does not constitute a cloud evaluation. However, this comparison (in addition to the comparison of the water contents) helps us identify the possible origins of the cloudy RHR biases, even though we cannot determine whether the cloud fraction differences are biases or not.

In the models, the clouds tend to produce too little warming in the low and middle levels and too much warming (too little cooling) in the high levels. For SW radiation, the larger amount of modeled clouds compared to the observations around 200 hPa generates slightly more SW warming in the vicinity of the clouds, meaning that ice cirrus clouds absorb more than they reflect solar radiation in this case (e.g., McFarlane 2008), while they significantly reduce the warming of underneath levels. On the contrary, the lack of clouds compared to the observations in the lower levels reduces the shortwave reflection in the vicinity of clouds and allows more absorption in the underneath levels. For LW radiation, the warming effect of clouds around 200 hPa is overestimated mostly due to the larger modeled IWC, whereas it is largely underestimated at the middle and low levels in deep convective regions (10˚S to 15˚N), far beyond the maximum uncertainty estimates. Poleward 10˚S to 15˚N, the smaller amount of low-level clouds associated to their lower height (identified as a bias in previous studies, e.g., Cesana and Waliser, 2016, Nam et al., 2012) generates more cooling rather than warming as opposed to the observations.

In addition, clear sky RHR differences between the 2BFL product and the models mitigate cloudy RHR biases in the low levels while they enhance them in the high levels (Fig. 4-5-6, bottom row, and Fig. 8). The models' lack of moisture over ocean in the tropics (e.g., Gonzalez and Jiang, 2017, John and Soden, 2007) lead to significant errors in LW radiation. Moreover, variations of the temperature profiles may cause up to 0.6 K/day differences in the clear sky LW RHR. In addition, these discrepancies may partly result from an overestimate the aerosol absorption and underestimate the biomass burning in the models (e.g. Matus et al., 2015), which affects mostly the SW radiation.

Finally, the RHR biases highlighted in this study are likely to cause cloud biases by modifying environmental parameters and contributing to changes in the large-scale circulation. For example, the warming of the upper levels may modify the convection (e.g., Li et al., 2016). On the contrary, the lack of warming near the surface and in the low levels probably prevents the clouds to lift up high enough and act as a feedback to nourish the cloud biases (e.g., Brient and Bony, 2012). Therefore, more work should be accomplished toward characterizing and quantifying cloud biases using combined CALIPSO-CloudSat product through the use of simulators, which allows a consistent evaluation. Such studies would allow us to better address cloud biases and determine whether the cloud differences found in this study are actual biases or not. Subsequently, one could examine the consequences of these biases on the radiative heating rates more precisely, ultimately improving the representation of cloud-radiation interactions and modeled cloud-climate feedback.

For example, we show that when the models simulate cloud profiles similar to the observations, i.e., at midlatitudes (Fig. 6), the RHR biases are substantially reduced. In addition, a better representation of cloud properties is also mandatory although the cloud frequency remains the main contributor to the RHR bias.

ACKNOWLEDGMENTS

GC was supported by a contract with the National Aeronautics and Space Administration, ROSES 2012, Earth Science Program, Modeling, Analysis and Prediction Program, at the Jet Propulsion Laboratory, © 2016 California Institute of Technology, and by a CloudSat-CALIPSO RTOP at the Goddard Institute for Space Studies. CALIPSO-GOCCP observations were downloaded from the CFMIP-Obs website (http://climserv.ipsl.polytechnique.fr/cfmip-obs/Calipso_goccp.html). CloudSat-CALIPSO-MODIS heating rate profiles and cloud profiles are available on the CloudSat website (http://www.cloudsat.cira.colostate.edu/data-products/level-2b/). CCCM data were obtained from the NASA Langley Research Center Atmospheric Science Data Center. The CMIP5 outputs can be found on the World Data Center for Climate (WDCC) website [http://cera-www.dkrz.de/]. The GASS-YoTC outputs can be made available upon request. The authors thank Seung-Hee Ham for her help with the processing of CCCM data and Tyler Thorsen for his help on interpreting differences between spaceborne and ground-based RHR. In addition, the authors are grateful to the editor and the three anonymous reviewers who provided valuable insights and helped us improve the manuscript.

REFERENCES

Ackerman, T. P., et al., “Heating rate in tropical anvils”. J. Atmos. Sci., 45, 1606–1623, (1988) doi:10.1175/1520-0469(1988)045<1606:HRITA>2.0.CO;2

Ackerman, S.A., R.E. Holz, R. Frey, E.W. Eloranta, B.C. Maddux, and M. McGill, 2008: Cloud Detection with MODIS. Part II: Validation. J. Atmos. Oceanic Technol., 25,1073–1086, https://doi.org/10.1175/2007JTECHA1053.1

Austin, R. T., A. J. Heymsfield, and G. L. Stephens, (2009) Retrieval of ice cloud microphysical parameters using the CloudSat millimeter-wave radar and temperature, J. Geophys. Res., 114, D00A23, doi:10.1029/2008JD010049.

Bony, S., M. Webb, C. Bretherton, S. Klein, P. Siebesma, G. Tselioudis, and M. Zhang (2011), CFMIP: Towards a better evaluation and understanding of clouds and cloud feedbacks in CMIP5 models, CLIVAR Exchanges, 56, International CLIVAR Project Office, Southampton, United Kingdom, 20–24.

Brient, F., and S. Bony, “How may low-cloud radiative properties simulated in the current climate influence low-cloud feedbacks under global warming?”, Geophys. Res. Lett., 39, L20807, (2012), doi:10.1029/2012GL053265.

Cesana G., et al., “Using in-situ airborne measurements to evaluate three cloud phase products derived from CALIPSO”, J. Geophys. Res. Atmos., 121, (2016), doi:10.1002/2015JD024334.

Cesana, G., and H. Chepfer (2012), How well do climate models simulate cloud vertical structure? A comparison between CALIPSO-GOCCP satellite observations and CMIP5 models, Geophys. Res. Lett., doi : 10.1029/2012GL053153

Cesana G. and D. E. Waliser, 2016: Characterizing and understanding systematic biases in the vertical structure of clouds in CMIP5/CFMIP2 models, *Geophys. Res. Let.*, Accepted, doi: 10.1002/2016GL070515

Chepfer H., et al., "The GCM Oriented Calipso Cloud Product (CALIPSO-GOCCP)", J. Geophys. Res., (2010), doi: 10.1029/2009JD012251

Chepfer, H., S. Bony, D. M. Winker, M. Chiriaco, J.-L. Dufresne, and G. Seze (2008), Use of CALIPSO lidar observations to evaluate the cloudiness simulated by a climate model, Geophys. Res. Lett., 35, L15704, doi:10.1029/2008GL034207

DeAngelis A, X Qu, MD Zelinka, and A Hall, 2015: An observational radiative constraint on hydrologic cycle intensification. *Nature*, 528, 249-253. DOI: 10.1038/nature15770.

Deng, M., G.G. Mace, Z. Wang, and R.P. Lawson, 2013: Evaluation of Several A-Train Ice Cloud Retrieval Products with In Situ Measurements Collected during the SPARTICUS Campaign. J. Appl. Meteor. Climatol., 52, 1014–1030, https://doi.org/10.1175/JAMC-D-12-054.1

Fu, Q., and K. N. Liou (1992), On the correlated k-distribution method for radiative transfer in nonhomogeneous atmospheres, J. Atmos. Sci., 49, 2139–2156.

Gonzalez, A. O., and X. Jiang (2017), Winter mean lower tropospheric moisture over the Maritime Continent as a climate model diagnostic metric for the propagation of the Madden-Julian oscillation, Geophys. Res. Lett., 44, 2588–2596, doi:10.1002/2016GL072430.

Ham, S.-H., S. Kato, F. G. Rose, D. Winker, T. L'Ecuyer, G. G. Mace, D. Painemal, S. Sun-Mack, Y. Chen, and W. F. Miller (2017), Cloud occurrences and cloud radiative effects (CREs) from CERES-CALIPSO-CloudSat-MODIS (CCCM) and CloudSat radar-lidar (RL) products, J. Geophys. Res. Atmos., 122, 8852–8884, doi:10.1002/2017JD026725.

Haynes, J. M., T. H. Vonder Haar, T. L'Ecuyer, and D. Henderson (2013), Radiative heating characteristics of Earth's cloudy atmosphere from vertically resolved active sensors, Geophys. Res. Lett., 40, 624–630, doi:10.1002/grl.50145

Henderson, D. S., et al., "A multisensor perspective on the radiative impacts of clouds and aerosols". J. Appl. Meteor. Climatol., 52, 853–871, (2013), doi:10.1175/JAMC-D-12-025.1.

Hourdin, F., T. Mauritsen, A. Gettelman, J. Golaz, V. Balaji, Q. Duan, D. Folini, D. Ji, D. Klocke, Y. Qian, F. Rauser, C. Rio, L. Tomassini, M. Watanabe, and D. Williamson, (2016), The art and science of climate model tuning**.** Bull. Amer. Meteor. Soc. doi:10.1175/BAMS-D-15-00135.1

Jiang, X., et al. (2015), Vertical structure and physical processes of the Madden-Julian oscillation: Exploring key model physics in climate simulations, J. Geophys. Res. Atmos., 120, doi:10.1002/2014JD022375

John, V. O.*, and* B. J. Soden *(*2007*)*, Temperature and humidity biases in global climate models and their impact on climate feedbacks, Geophys. Res. Lett., 34*, L18704, doi:*10.1029/2007GL030429**.**

Kato, S., S. Sun-Mack, W. F. Miller, F. G. Rose, Y. Chen, P. Minnis, and B. A. Wielicki, 2010: Relationships among cloud occurrence frequency, overlap, and effective thickness derived from CALIPSO and CloudSat merged cloud vertical profiles, J. Geophys. Res., 115, D00H28, doi:10.1029/2009JD012277.

Kato, S., Loeb, N.G., Rutan, D.A. et al. 2012: Uncertainty Estimate of Surface Irradiances Computed with MODIS-, CALIPSO-, and CloudSat-Derived Cloud and Aerosol Properties, Surv Geophys, 33(3-4), 395-412, https://doi.org/10.1007/s10712-012-9179-x

King, M. D., and Coauthors, 2003: Cloud and aerosol properties, precipitable water, and profiles of temperature and water vapor from MODIS. IEEE Trans. Geosci. Remote Sens., 41, 442–458, doi:10.1109/TGRS.2002.808226.

Kishore, P., Ratnam, M. V., Namboothiri, S., Velicogna, I., Basha, G., Jiang, J., Igarashi, K., Rao, S., and Sivakumar, V.: Global (50S– 50N) distribution of water vapor observed by COSMIC GPS RO: Comparison with GPS radiosonde, NCEP, ERA-Interim, and JRA-25 reanalysis data sets, J. Atmos. Solar-Terr. Phys., pp. 1849–1860, doi:10.1016/j.jastp.2011.04.017, 2011.

Klingaman, N. P., X. Jiang, P. K. Xavier, J. Petch, D. Waliser, and S. J. Woolnough, 2015: Vertical structure and physical processes of the Madden-Julian oscillation: Synthesis and summary. Journal of Geophysical Research: Atmospheres, 120, 10.1002/2015JD023196, 4671-4689.

L'Ecuyer et al., "Impact of clouds on atmospheric heating based on the R04 CloudSat fluxes and heating rates data set", JGR, (2008), doi:10.1029/2008JD009951

Li, J.-L. F., et al. (2012), An observationally based evaluation of cloud ice water in CMIP3 and CMIP5 GCMs and contemporary reanalyses using contemporary satellite data, J. Geophys. Res., 117, D16105, doi:10.1029/2012JD017640.

Li, J.-L. F., W.-L. Lee, D. Waliser, Y.-H. Wang, J.-Y. Yu, X. Jiang, T. L'Ecuyer, Y.-C. Chen, T. Kubar, E. Fetzer, et al. (2016), Considering the radiative effects of snow on tropical Pacific Ocean radiative heating profiles in contemporary GCMs using A-Train observations, J. Geophys. Res. Atmos., 121, 1621–1636, doi:10.1002/2015JD023587.

Mace, J., and F. J. Wrenn (2013), Evaluation of the Hydrometeor Layers in the East and West Pacific within ISCCP Cloud-Top Pressure–Optical Depth Bins Using Merged CloudSat and CALIPSO Data, *J. Climate*, *26*, 9429-9444, doi:10.1175/JCLI-D-12-00207.1.

Mather, J. H., S. A. McFarlane, M. A. Miller, and K. L. Johnson (2007), Cloud properties and associated radiative heating rates in the tropical western Pacific, J. Geophys. Res., 112, D05201, doi:10.1029/2006JD007555

Matus, A., T. L'Ecuyer, J. Kay, C. Hannay, and J. Lamarque, 2015: The role of clouds in modulating global aerosol direct radiative effects in spaceborne active observations and the community earth system model, *J. Climate*, 28, 2986-3003

Matus, A. V. and T. S. L'Ecuyer, 2017: The role of cloud phase in Earth's radiation budget, *J. Appl. Meteor. and Climatol.*, in press.

Minnis, P., et al., 2008: Cloud detection in nonpolar regions for CERES using TRMM VIRS and Terra and Aqua MODIS data, IEEE Trans. Geosci. Remote Sens., 46, 3857–3884, doi:10.1109/TGRS.2008. 2001351.

Minnis, P., et al., 2011: CERES edition-2 cloud property retrievals using TRMM VIRS and Terra and Aqua MODIS data—Part I: Algorithms, IEEETrans. Geosci. Remote Sens., 49, 4374–4400, doi:10.1109/TGRS.2011.2144601.

Mülmenstädt, J., Sourdeval, O., Henderson, D. S., L'Ecuyer, T. S., Unglaub, C., Jungandreas, L., Böhm, C., Russell, L. M., and Quaas, J., 2018, : Using CALIOP to estimate cloud-field base height and its uncertainty: the Cloud Base Altitude Spatial Extrapolator (CBASE) algorithm and dataset, Earth Syst. Sci. Data Discuss., Accepted

Oreopoulos, L., N. Cho, D. Lee, and S. Kato, 2016: Radiative effects of global MODIS cloud regimes, J. Geophys. Res. Atmos., 121, 2299–2317, doi:10.1002/2015JD024502.

Protat, A., S. A. Young, S. A. McFarlane, T. L'Ecuyer, G. G. Mace, J. M. Comstock, C. N. Long, E. Berry, and J. Delanoë (2014), Reconciling ground-based and space-based estimates of the frequency of occurrence and radiative effect of clouds around Darwin, Australia, J. Appl. Meteor. Climatol., 53, 456–478, doi:10.1175/JAMC-D-13-072.1.

Sassen, K., and Z. Wang, (2008) Classifying clouds around the globe with the CloudSat radar: 1-year of results, Geophys. Res. Lett., 35, L04805, doi:10.1029/2007GL032591.

Shindell, D. T., and Coauthors, 2013: Radiative forcing in the ACCMIP historical and future climate simulations. Atmos. Chem. Phys., 13, 2939–2974, doi:10.5194/acp-13-2939-2013

Simmons, A. J., K. M. Willett, P. D. Jones, P. W. Thorne, and D. P. Dee (2010), Low-frequency variations in surface atmospheric humidity, temperature, and precipitation: Inferences from reanalyses and monthly gridded observational data sets, J. Geophys. Res., 115, D01110, doi:10.1029/2009JD012442.

Stackhouse, P. W.,D. P. Kratz, G. R. McGarragh, S. K. Gupta, and E. B. Greer, 2006: Fast longwave and shortwave flux (FLASHflux) products from CERES and MODIS measurements. Preprints, 12th Conf. on Atmospheric Radiation, Madison, WI, Amer. Meteor. Soc., P1.10. [Available online at http://ams.confex.com/ams/pdfpapers/113479.pdf.]

Sun, W., G. Videen, S. Kato, B. Lin, C. Lukashin, and Y. Hu, 2011: A study of subvisual clouds and their radiation effect with a synergy of CERES, MODIS, CALIPSO, and AIRS data, J. Geophys. Res., 116, D22207, doi:10.1029/2011JD016422.

Stephens G. L., et al., “The CloudSat Mission and the A-Train”. Bull. Amer. Meteor. Soc. 83, 1771-1790, (2002).

Stephens, G. L., et al., “An update on Earth’s energy balance in light of the latest global observations”, Nat. Geosci., 5, 691–696, (2012).

Taylor, K.E., R.J. Stouffer, G.A. Meehl, 2012: An Overview of CMIP5 and the experiment design.” Bull. Amer. Meteor. Soc., 93, doi:10.1175/BAMS-D-11-00094.1.

Trenberth KE, Fasullo JT, Kiehl J. 2009. Earth's global energy budget. Bull. Am. Meteorol. Soc. 90: 311–323.

Vaughan, M., K. Powell, R. Kuehn, S. Young, D. Winker, C. Hostetler, W. Hunt, Z. Liu, M. McGill, and B. Getzewich, “Fully Automated Detection of Cloud and Aerosol Layers in the CALIPSO Lidar Measurements”, J. Atmos. Oceanic Technol., vol 26, pp. 2034–2050, 2009.

Wielicki B.A., et al. (1996), Clouds and the Earth’s Radiant Energy System (CERES): An earth observing system experiment. Bull. Amer. Meteor. Soc., 77, 853–868.

Winker, D. M., J. P., J. A. Coakley Jr., S. A. Ackerman, R. J. Charlson, P. R. Colarco, P. Flamant, Q. Fu,R. M. Hoff, C. Kittaka, T. L. Kubar, H. Le Treut, M. P. McCormick, G. Mégie, L. Poole, K. Powell, C. Trepte, M. A. Vaughan, and B. A. Wielicki, (2010), The CALIPSO Mission: A Global 3D View of Aerosols and Clouds. Bull. Amer. Meteor. Soc., 91, 1211–1229, doi: 10.1175/2010BAMS3009.1

Wild, M., 2012: New Directions: A facelift for the picture of the global energy balance. Atmospheric Environment, 55, 366-367

Zhao, G., and L. Di Girolamo, 2006: Cloud fraction errors for trade wind cumuli from EOS Terra instruments. Geophys. Res. Lett., 33, L20802, doi:10.1029/2006GL027088.

TABLES

Table 1: List of perturbations performed with the 2BFL algorithm for the uncertainty analysis. See H13 for more details about the experiment setup.

	Parameter	Perturbation
CALIPSO	IWC	2x / ÷2
	LWC	±20%
	Liquid Reff	±3μm
	Ice Reff	±10μm
	AOD	2x / ÷2
CloudSat	IWC	±70%
	LWC	±50%
	Liquid Reff	±25%
	Ice Reff	±25%
Environmental properties	Specific Humidity	±25%
	Temperature	±2K

FIGURE CAPTIONS

FIGURE 1: Sensitivity of profiles (y-axis, pressure [hPa]) of the 2BFL LW, SW and net RHR (x-axis, K/day) to perturbations in the input parameters for August 2007. The two left, middle and right columns represent the LW (left) and SW (right) RHR profiles in all, clear and cloudy sky conditions for three cloud regimes (described in section 2.2 and 4.1): tropical convection ($\omega500 <$ -10 hPa/day, between 30˚S/N; top row), tropical subsidence ($\omega500 >$ 10 hPa/day; between 30˚S/N; middle row) and midlatitudes (all ω500 between 30˚S/N and 50˚S/N; bottom row). The light grey and dark grey shading correspond to the maximum uncertainty estimates – i.e., the square root of the sum of square uncertainties – computed from all parameters and cloud parameters only, respectively. Solid and dashed lines designate to positive and negative perturbations while the reddish, bluish and greenish colors correspond to liquid, ice and environmental parameters, respectively. See the legend and Table 1 for the exact parameter's names and section 2.2 for more detail about the uncertainty analysis. Note that, in clear sky, the impact of environmental perturbations (i.e., humidity and temperature) on RHR are large whereas they do not have as much impact when a cloud is present, generating a smaller uncertainty.

FIGURE 2: Zonal profiles (x-axis, latitude [˚N]; y-axis, pressure [hPa]) of RHR maximum uncertainty estimates (K/day) derived from Table 1 perturbations, i.e., the square root of the sum of all square uncertainties. The top, middle and bottom row correspond to LW, SW and net radiation while the left, middle and right column correspond to all, clear and cloudy sky conditions, respectively. Note that the range is different for SW radiation.

FIGURE 3: Zonal profiles (x-axis, latitude [˚]; y-axis, height [km]) of Cloud Frequency (CF, %) a) as observed by CloudSat-CALIPSO (RL-Geoprof R04, 2007-2010 daytime and nighttime,

monthly mean), b) as simulated by 5 GASS-YOTC models (2002-2005, monthly means), along with c) the standard deviation of the difference between the multimodel mean and the observations and d) the difference between the multimodel mean and the observations.

FIGURE 4: Profiles (y-axis, pressure [hPa]) of observed and modeled LW, SW and net RHR (from left to right; x-axis, K/day) in all, clear and cloudy sky conditions (from top to bottom) for tropical convection, i.e., $\omega500 < -10$ hPa/day, between 30˚S/N. To facilitate the interpretation of cloudy sky RHR biases, the observed and modeled cloud fraction and IWC/LWC profiles are also shown in the top right corner (d). Note that there are no uncertainty estimates for the observed CF (2007-2010) and IWC/LWC (2010). Their modeled counterparts are averaged over a 4-year long time period (2002-2005) and the shadings correspond to the multimodel standard deviations. The 2BFL observations (2007-2010) are represented in orange. Their uncertainty estimates are computed from the same data as in Fig. 2 but for the specific region and regime used here. The merged CCCM+2BFL observations (2007-2010) and its standard deviation are in purple. The multimodel mean and standard deviation (1991-2008) are shown in green.

FIGURE 5: Same as Fig. 4 but for tropical subsidence, i.e., $\omega500 > 10$ hPa/day, between 30˚S/N.

FIGURE 6: Same as Fig. 4 for midlatitudes, i.e., all ω500 between 30˚S/N and 50˚S/N.

FIGURE 7: Zonal profiles (x-axis, latitude [˚]; y-axis, pressure [hPa]) of annual mean RHR (K/day) for the 2BFL observations (left column, 2007-2010 daytime and nighttime, monthly files) for the multimodel mean (5 models, 1991-2008, middle column) and the multimodel mean bias (right column). The rows correspond to the LW, SW and net radiation from the top to the bottom. Horizontal black dashed lines separate the low- and mid-level clouds (680 hPa), and mid- and high-level clouds (440 hPa). The red and blue shading designate cooling and warming,

respectively. To highlight significant model error estimates in Fig. 7-8-9, only biases larger than the observed maximum uncertainty estimates are shown (right columns). Note that the SW RHR (and bias) has a different range compared to the LW and net RHR.

FIGURE 8: Same as Fig. 7 for clear sky conditions.

FIGURE 9: Same as Fig. 7 for cloudy sky conditions (defined as all sky minus clear sky).

FIGURE 1: Sensitivity of profiles (y-axis, pressure [hPa]) of the 2BFL LW, SW and net RHR (x-axis, K/day) to perturbations in the input parameters for August 2007. The two left, middle and right columns represent the LW (left) and SW (right) RHR profiles in all, clear and cloudy sky conditions for three cloud regimes (described in section 2.2 and 4.1): tropical convection ($\omega 500 <$ -10 hPa/day, between 30˚S/N; top row), tropical subsidence ($\omega 500 >$ 10 hPa/day; between 30˚S/N; middle row) and midlatitudes (all $\omega 500$ between 30˚S/N and 50˚S/N; bottom row). The light grey and dark grey shading correspond to the maximum uncertainty estimates – i.e., the square root of the sum of square uncertainties – computed from all parameters and cloud parameters only, respectively. Solid and dashed lines designate to positive and negative perturbations while the reddish, bluish and greenish colors correspond to liquid, ice and environmental parameters, respectively. See the legend and Table 1 for the exact parameter's names and section 2.2 for more detail about the uncertainty analysis. Note that, in clear sky, the impact of environmental perturbations (i.e., humidity and temperature) on RHR are large whereas they do not have as much impact when a cloud is present, generating a smaller uncertainty.

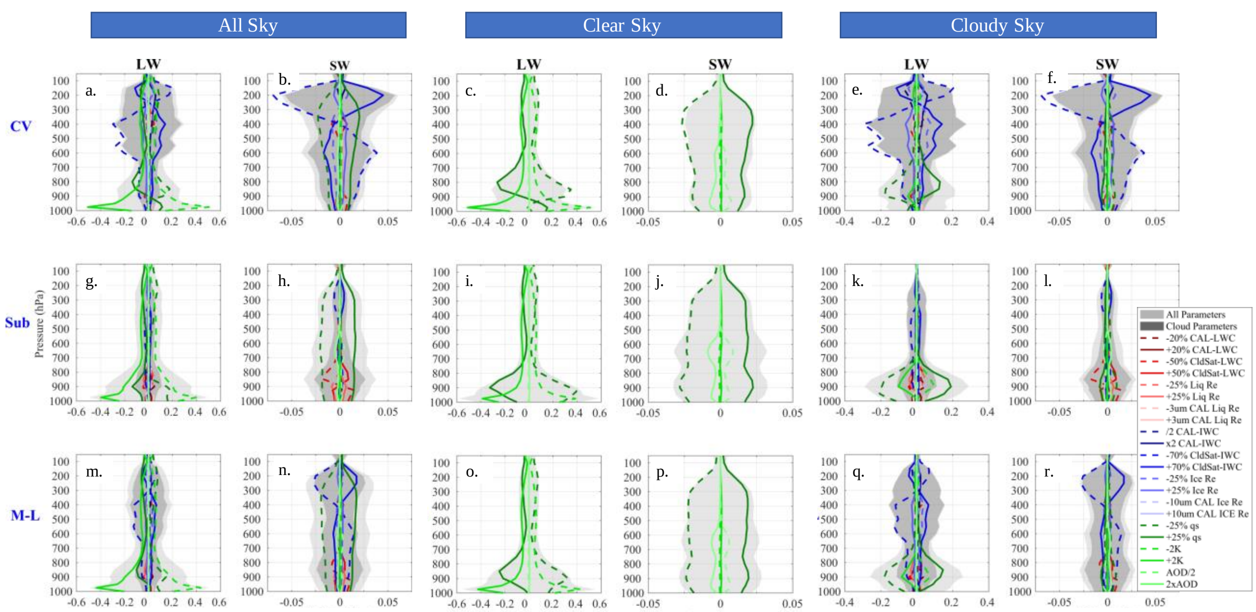

FIGURE 2: Zonal profiles (x-axis, latitude [˚N]; y-axis, pressure [hPa]) of RHR maximum uncertainty estimates (K/day) derived from Table 1 perturbations, i.e., the square root of the sum of all square uncertainties. The top, middle and bottom row correspond to LW, SW and net radiation while the left, middle and right column correspond to all, clear and cloudy sky conditions, respectively. Note that the range is different for SW radiation.

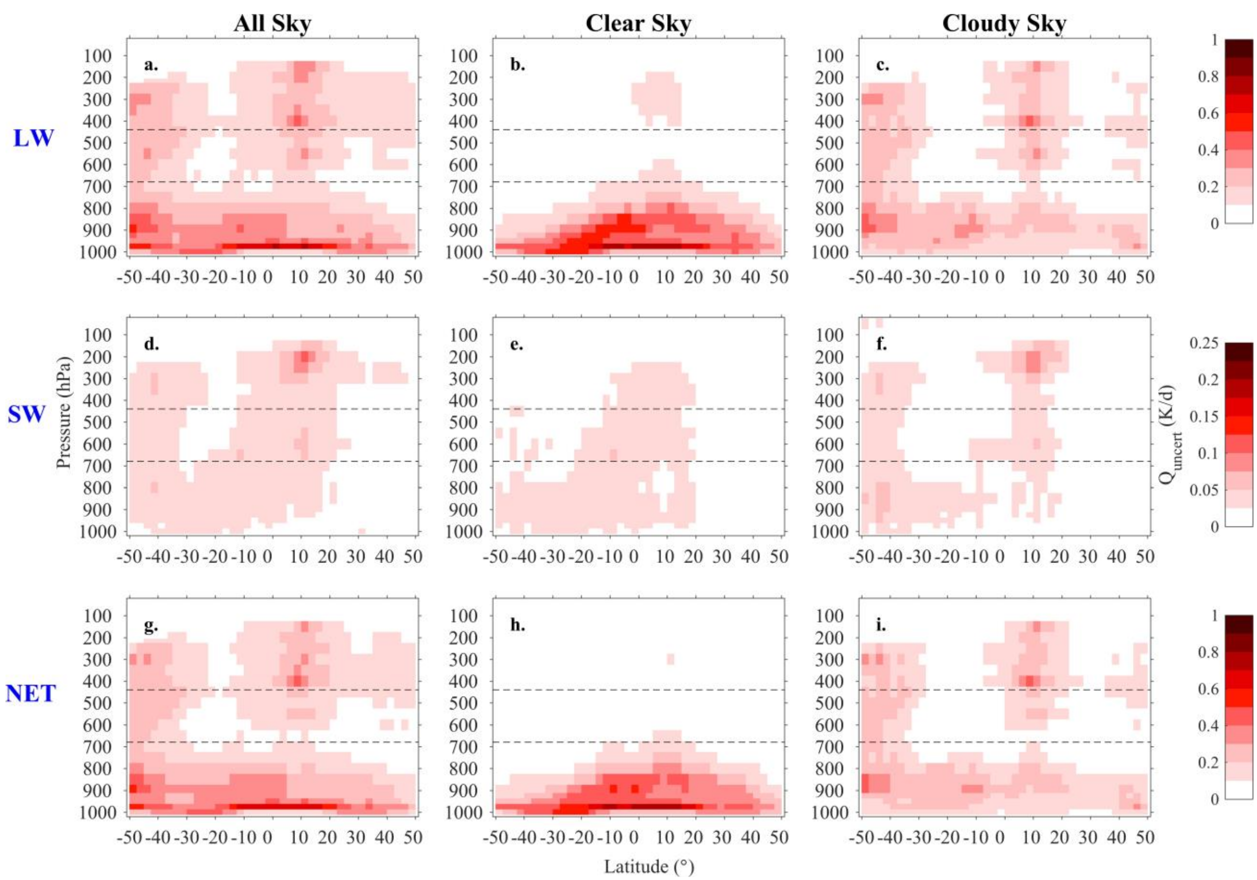

FIGURE 3: Zonal profiles (x-axis, latitude [˚]; y-axis, height [km]) of Cloud Frequency (CF, %) a) as observed by CloudSat-CALIPSO (RL-Geoprof R04, 2007-2010 daytime and nighttime, monthly mean), b) as simulated by 5 GASS-YOTC models (2002-2005, monthly means), along with c) the standard deviation of the difference between the multimodel mean and the observations and d) the difference between the multimodel mean and the observations.

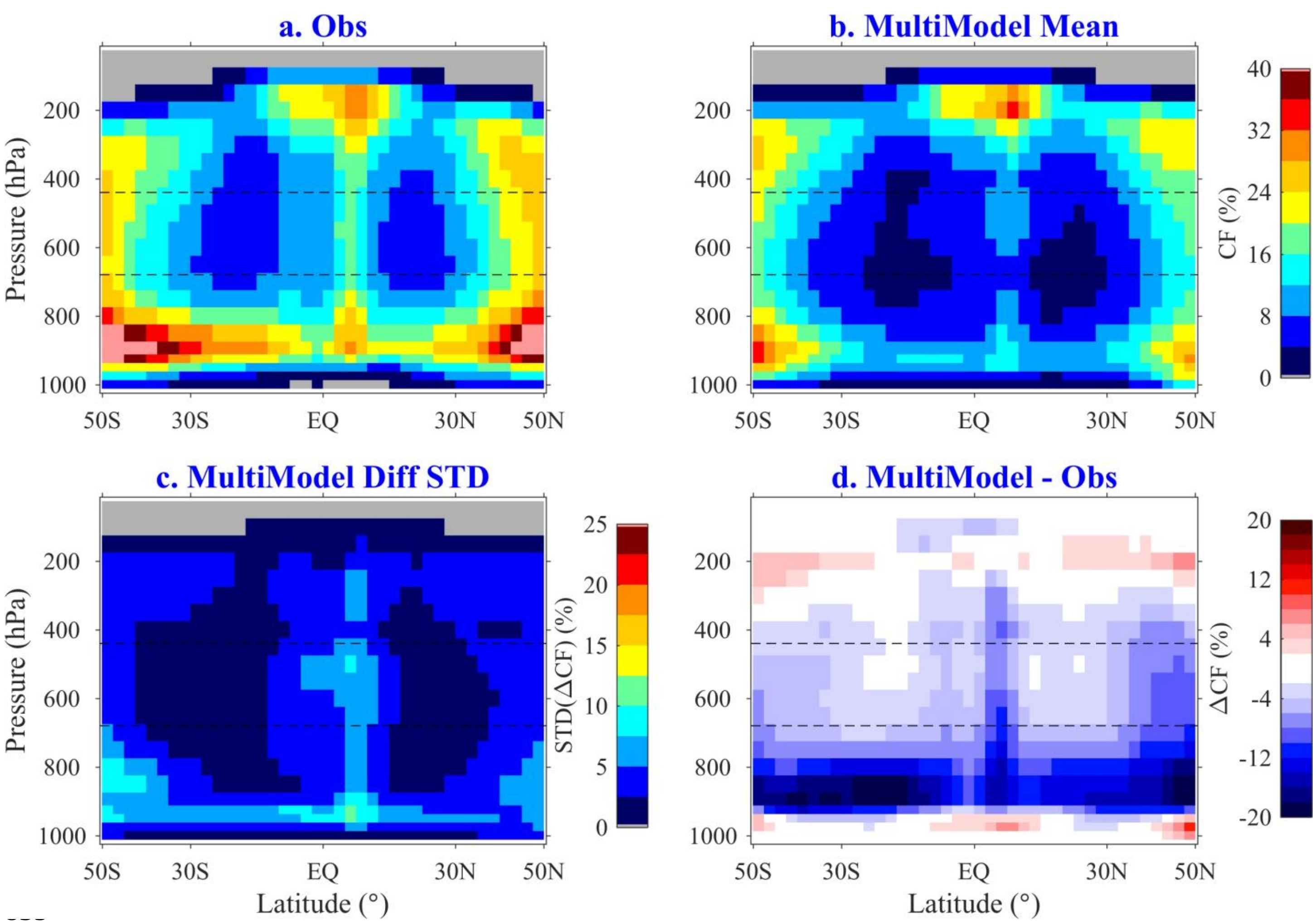

FIGURE 4: Profiles (y-axis, pressure [hPa]) of observed and modeled LW, SW and net RHR (from left to right; x-axis, K/day in all, clear and cloudy sky conditions (from top to bottom) for tropical convection, i.e., ω500 < -10 hPa/day, between 30˚S/N. To facilitate the interpretation of cloudy sky RHR biases, the observed and modeled cloud fraction and IWC/LWC profiles are also shown in the top right corner (d). Note that there are no uncertainty estimates for the observed CF (2007-2010) and IWC/LWC (2010). Their modeled counterparts are averaged over a 4-year long time period (2002-2005) and the shadings correspond to the multimodel standard deviations. The 2BFL observations (2007-2010) are represented in orange. Their uncertainty estimates are computed from the same data as in Fig. 2 but for the specific region and regime used here. The merged CCCM+2BFL observations (2007-2010) and its standard deviation are in purple. The multimodel mean and standard deviation (1991-2008) are shown in green.

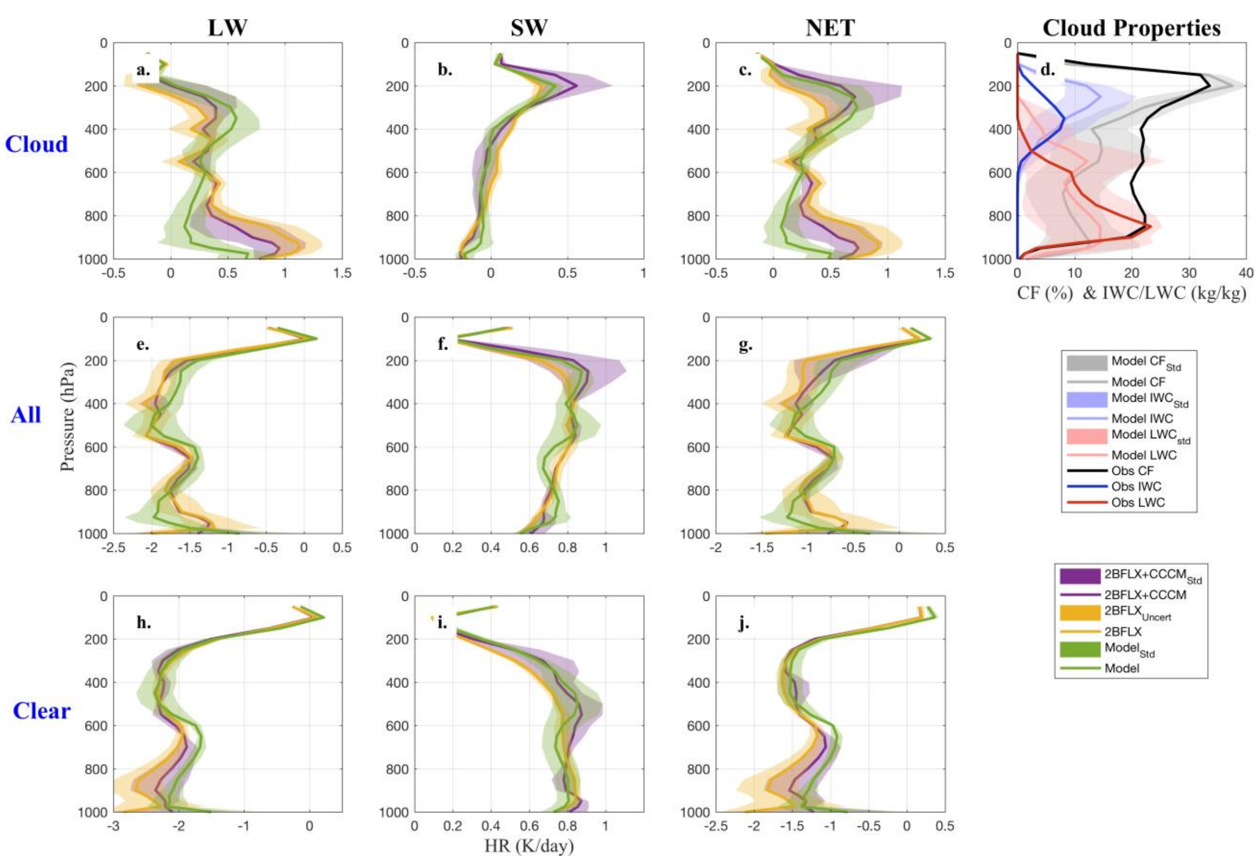

FIGURE 5: Same as Fig. 4 but for tropical subsidence, i.e., ω500 > 10 hPa/day, between 30˚S/N.

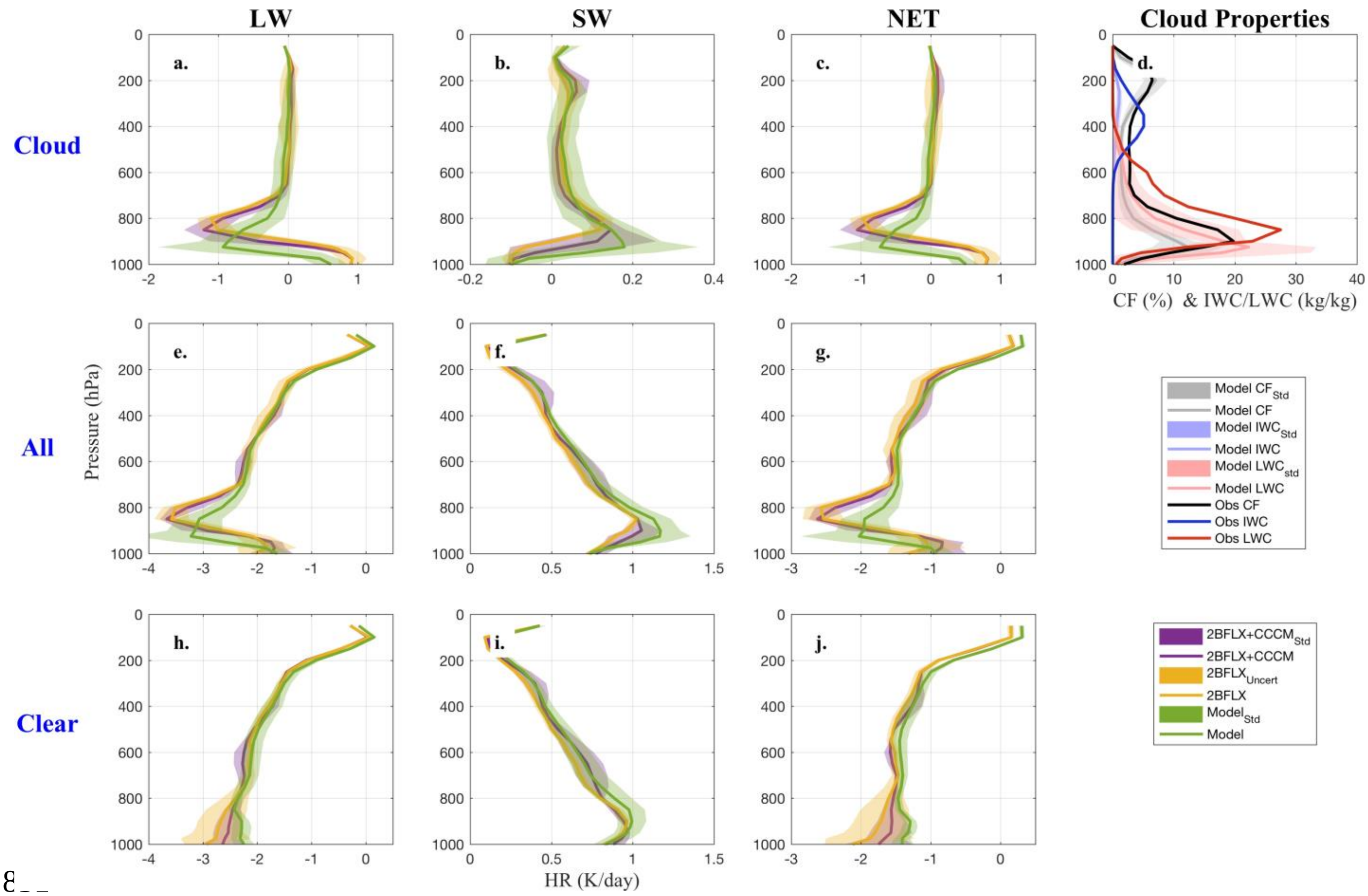

FIGURE 6: Same as Fig. 4 for midlatitudes, i.e., all ω500 between 30˚S/N and 50˚S/N.

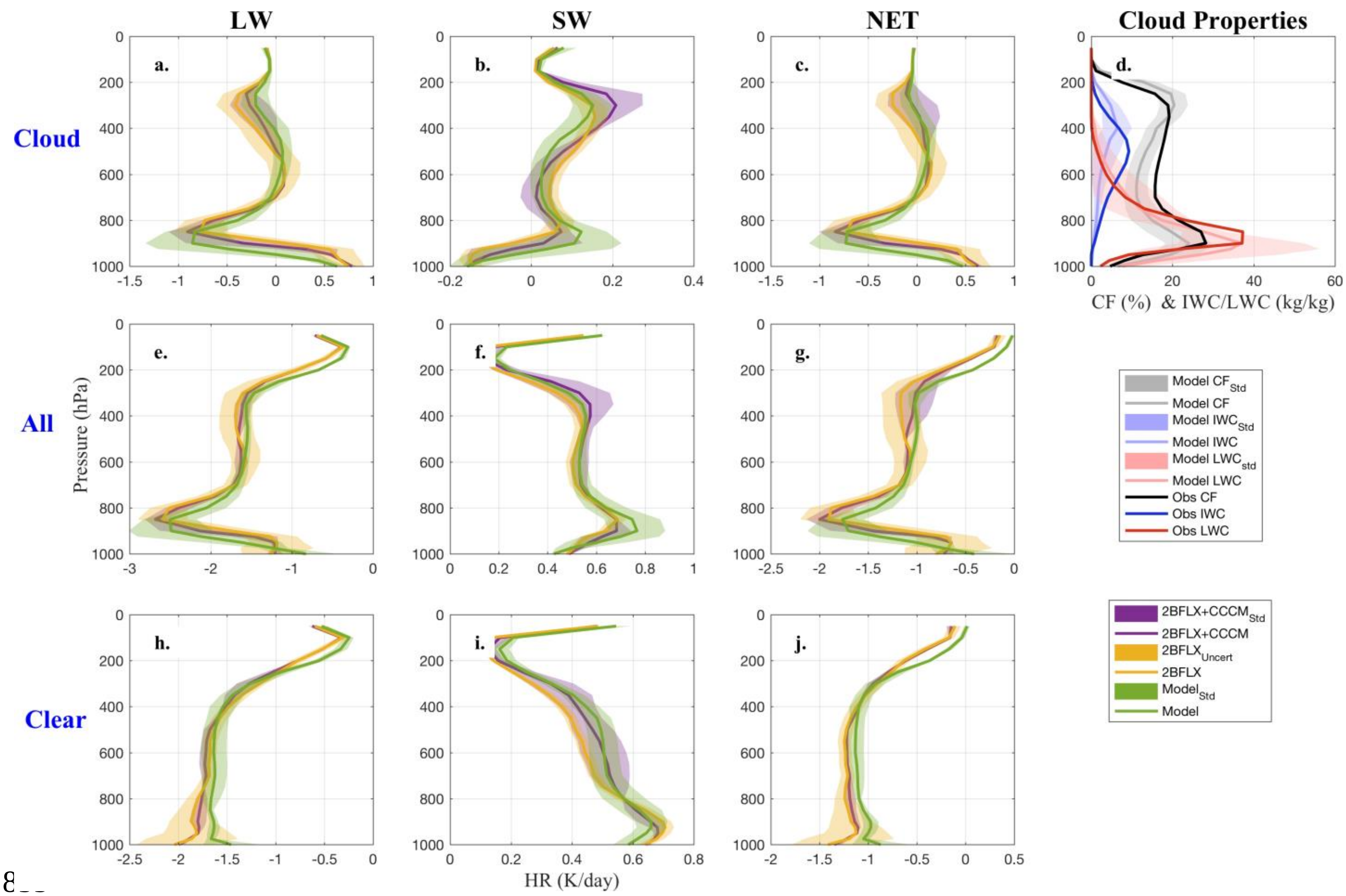

FIGURE 7: Zonal profiles (x-axis, latitude [˚]; y-axis, pressure [hPa]) of annual mean RHR (K/day) for the 2BFL observations (left column, 2007-2010 daytime and nighttime, monthly files) for the multimodel mean (5 models, 1991-2008, middle column) and the multimodel mean bias (right column). The rows correspond to the LW, SW and net radiation from the top to the bottom. Horizontal black dashed lines separate the low- and mid-level clouds (680 hPa), and mid- and high-level clouds (440 hPa). The red and blue shading designate cooling and warming, respectively. To highlight significant model error estimates in Fig. 7-8-9, only biases larger than the observed maximum uncertainty estimates are shown (right columns). Note that the SW RHR (and bias) has a different range compared to the LW and net RHR.

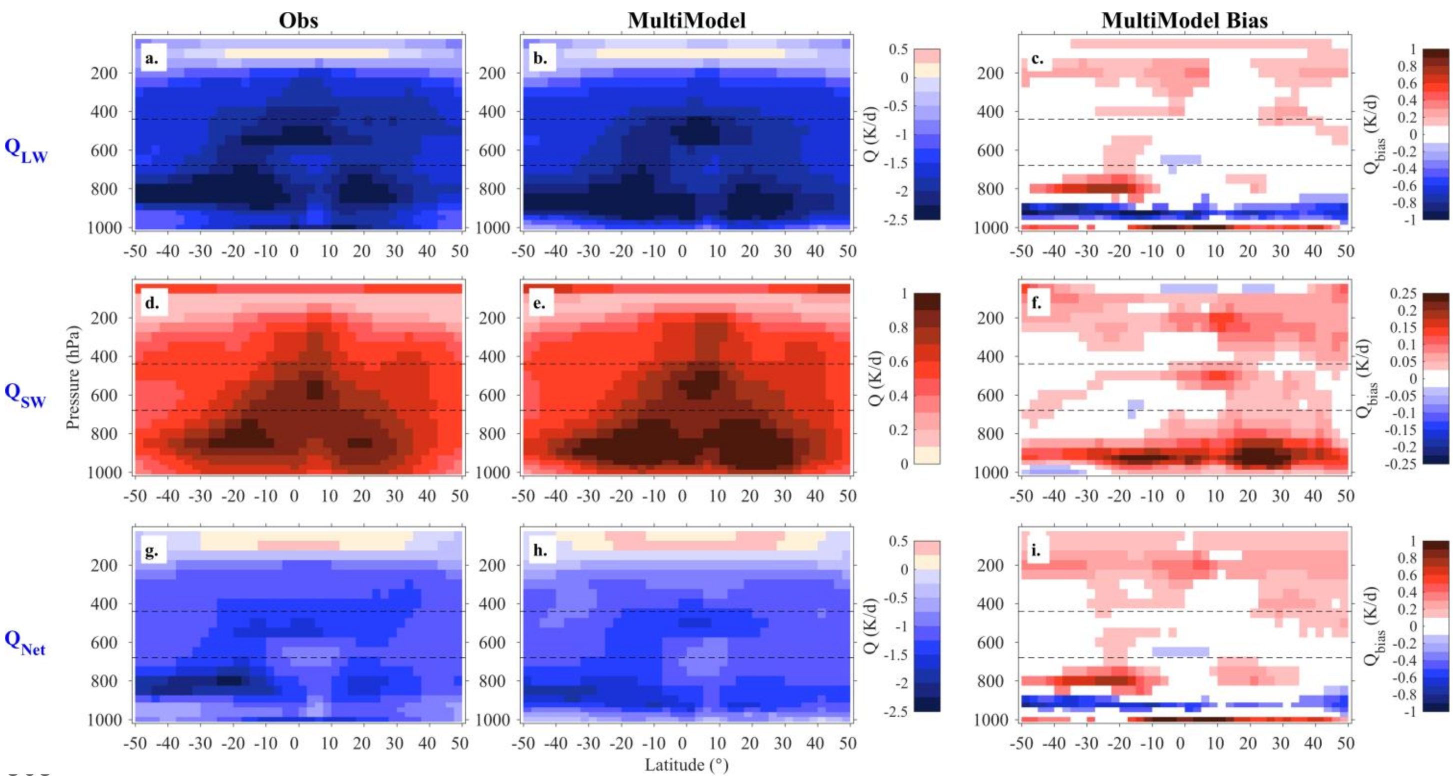

FIGURE 8: Same as Fig. 7 for clear sky conditions.

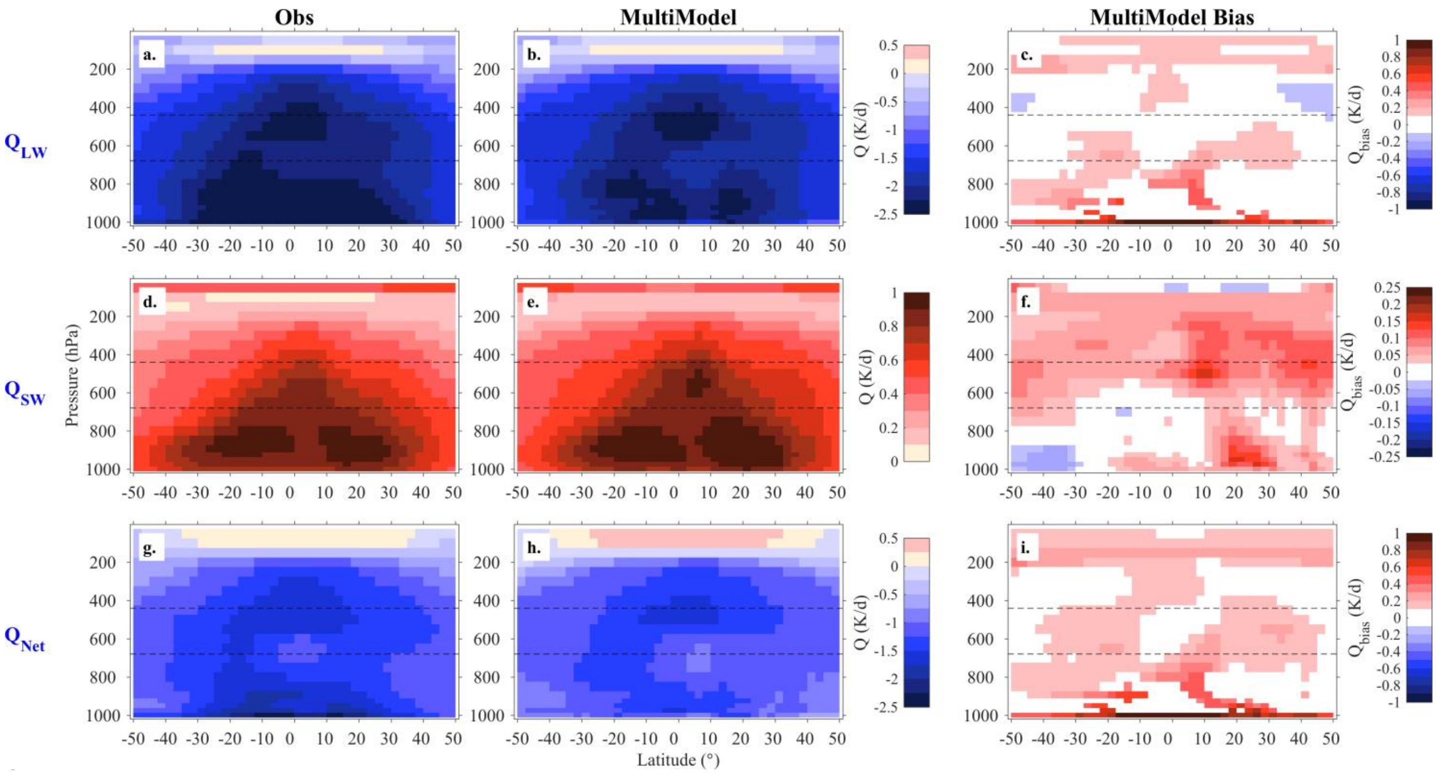

FIGURE 9: Same as Fig. 7 for cloudy sky conditions (defined as all sky minus clear sky).